LA-UR-24-21522
Accepted Manuscript

Calibration and validation of the foundation for a multiphase strength model for tin

Nguyen, Thao Thi Tam; Fensin, Saryu Jindal; Luscher, Darby Jon; Prime, Michael Bruce; Burakovsky, Leonid; Cady, Carl Mcelhinney; Gray, George Thompson III; Jones, David Robert; Martinez, Daniel Tito; Rowland, Richard Lee II; Sjue, Sky K.; Sturtevant, Blake; Valdez, James Anthony

To be published in: Journal of Applied Physics

DOI to publisher's version: 10.1063/5.0207405

Permalink to record:
https://permalink.lanl.gov/object/view?what=info:lanl-repo/lareport/LA-UR-24-21522

Calibration and validation of the foundation for a multiphase strength model for tin

Thao Nguyen, Leonid Burakovsky, Saryu J. Fensin*, Darby J. Luscher*, Michael B. Prime*, Carl Cady, George T. Gray III, David R. Jones, Daniel T. Martinez, Richard L. Rowland, Sky Sjue, Blake T. Sturtevant, James A. Valdez

Los Alamos National Laboratory, Los Alamos, NM 87545, United States

---

Abstract

In this work, the Common Model of Multi-phase Strength and Equation of State (CMMP) model was applied to tin. Specifically, calibrations of the strength-specific elements of the CMMP foundation were developed with a combination of experiments and theory, and then the model was validated experimentally. The first element of the foundation is a multi-phase analytic treatment of the melt temperature and the shear modulus for the solid phases. These models were parameterized for each phase based on ab initio calculations using the software VASP (Vienna Ab initio Simulations Package) based on density functional theory (DFT). The shear modulus model for the ambient β phase was validated with ultrasonic sound speed measurements as a function of pressure and temperature. The second element of the foundation is a viscoplastic strength model for the β phase, upon which strength for inaccessible higher-pressure phases can be scaled as necessary. The stress-strain response of tin was measured at strain rates of 10^{-3} to 3×10^3 s^{-1} and temperatures ranging from 87 to 373 K. The Preston-Tonks-Wallace (PTW) strength model was fit to that data using Bayesian model calibration. For validation, six forward and two reverse Taylor impact experiments were performed at different velocities to measure large plastic deformation of tin at strain rates up to 10^5 s^{-1}. The PTW model accurately predicted the deformed shapes of the cylinders, with modest discrepancies attributed to the inability of PTW to capture the effects of twinning and dynamic recrystallization. Some material in the simulations of higher velocity Taylor cylinders reached the melting temperature, thus testing the multiphase model because of the presence of a second phase, the liquid. In simulations using a traditional modeling approach, the abrupt reduction of strength upon melt resulted in poor predictions of the deformed shape and non-physical temperatures. With CMMP, the most deformed material points evolved gradually to a mixed solid-liquid but never fully liquid state, never fully lost strength, stayed at the melt temperature as the latent heat of fusion was absorbed, and predicted the deformed shape well.

Keywords: tin, Taylor impact test, dynamic strength, large plastic deformation, multi-phase, mixed-phase, melt

Manuscript history:

Dated: May 14, 2024

---

1. Introduction

Actionable engineering assessments across a broad range of applications, including automotive, aerospace, biomedical, and defense, to name a few, require continuum constitutive models to represent the thermomechanical behavior of polycrystalline metals. In many of these applications, the relevant environmental conditions can include broad ranges of temperature, pressure, and deformation rate. Furthermore, under more extreme conditions, polycrystalline metals may change phase, including between solid polymorphs or between solid and liquid. Often the range of conditions a material may experience in-situ cannot be readily reproduced within controlled laboratory characterization experiments. Thus, models may be used to interpolate the dynamic behavior of materials between observable states or conditions that can be accessed in experiment, and in some cases extrapolate to conditions beyond their calibration.

Because of its relatively low melt temperature, and modest transformation pressures for some solid-solid phase transformations, tin enables exploration of dynamic deformation behavior across phase boundaries using different experimental platforms. (See [1], table I, for the five known solid phases of tin in or order of pressure.) Tin is stable in a body-centered tetragonal (BCT) β-tin polymorph at ambient temperature and pressure. Tin will readily transform to a higher density BCT γ-tin at moderate pressures, which can be achieved for example by impact loading in a laboratory gas gun. Tin can melt from relatively modest combinations of initial heating, shock heating, or heating from the work of plastic deformation. The even higher pressure δ and ϵ phases can be explored using pulsed power [2, 3] or laser drive [4]. Tin also has no significant toxicity or hazard issues, so it takes less time and resources to explore with many experiments.

Because of this readily accessible phase-space, tin has become an international *de facto* standard for studying *multiphase* thermomechanical behavior [5–18]. Simulation of the dynamic behavior observed in these and other experiments requires a multi-phase thermomechanical constitutive description of tin. While specific model calibrations

---

*Corresponding authors

Email addresses: `saryuj@lanl.gov` (Saryu J. Fensin), `djl@lanl.gov` (Darby J. Luscher), `prime@lanl.gov` (Michael B. Prime) for tin cannot be transferred directly to other materials, the developments in modeling and experiments for tin are invaluable for applications to other materials, especially those for which experiments are more expensive or phases are more difficult to access.

This paper calibrates and validates the strength-specific "foundation" for applying the Common Model of Multiphase Strength and Equation of State (CMMP) [19] to tin.[1] The CMMP [19] framework was recently developed to address the multiphysics problem of simulating multiphase strength along an arbitrary thermomechanical path. To put our work into context for the reader, we outline all the components of the CMMP. Then we explain why the portions we focus on here form the foundation of the strength modeling.

The CMMP is comprised of five main elements. We present them in approximately the calculational order of the model; although some calculations are coupled rather than sequential. The first two components concern phase identity and thermodynamics, are controlled by volumetric deformations as compared to deviatoric, and are not the main focus of this work. 1) Within each phase, the equation of state (EOS) gives the relationship between temperature, pressure, density, and internal energy for the material. Globally, it gives the equilibrium boundaries between all the phases. For a given material state, for example a density and temperature, the equilibrium state is identified by the EOS and may be mixed phase. Development and calibration of the EOS used in this work was reported separately [20]. 2) For dynamic loading, a model gives the non-equilibrium kinetics of each phase transition, for example, between β and γ phases [12, 21]. Kinetics models for tin are outside of the scope of the experiments presented in this work, and have received attention elsewhere [12, 19, 22].

The next two elements of the CMMP concern strength, are controlled by deviatoric (i.e., shear) deformations, and are the focus of the calibration efforts in this work. 3) Density and temperature-dependent shear moduli for each solid phase relate elastic deviatoric strains to deviatoric stresses. And 4) the flow stress, i.e., strength, behavior including effects of strain hardening, strain-rate, pressure, and temperature dependence is required for each phase. 5) The final element of the CMMP is a model to appropriately average properties and state variables for mixed phase regions. That element of the CMMP is not calibrated in this work but is exercised in the validation experiments.

The CMMP framework is modular, allowing different theoretical models to be used for any of these elements and for different phases. The modeling choices in this work are intended as a foundation for future refinements by broadly covering large regimes of temperature, pressure, strain, and strain rate.

The modeling approach for strength explains why we consider the shear modulus models part of the foundation for the strength model. Macroscopic strength models are often expressed as a scalar-valued flow stress within the context of a J_2 (i.e. the second invariant of the deviatoric stress) inelastic threshold surface. Some of these phenomenological models are expressed as a normalized flow stress in relation to the shear modulus such that $\tau = 2G(\rho, T)\hat{\tau}(\epsilon_\mathrm{p}, T, \dot{\epsilon}_\mathrm{p})$ where τ is the magnitude of the flow stress, ρ is the mass density per unit volume, T is the temperature, and ϵ_p, $\dot{\epsilon}_\mathrm{p}$ are the effective plastic strain and corresponding rate, respectively (e.g., [23–27]). $\hat{\tau}$ is a normalized flow stress, which is scaled by the appropriate value of shear modulus to fully define the density/pressure and temperature dependence of the plastic deformation behavior. That is why models for shear moduli for all phases is so important for the multiphase strength modeling.

Practicalities explain why an ambient phase strength model is the other main part of the foundation for the CMMP strength model. Calibration of a strength model is most directly obtained by parameterizing a particular model form $\hat{\tau}(\epsilon_\mathrm{p}, T, \dot{\epsilon}_\mathrm{p})$ to stress-strain curves from quasistatic (QS) uniaxial stress or dynamic split Hopkinson pressure bar (SHPB) experiments. However, it is often the case that only one (or a small subset) of all of the solid phases can be directly measured using QS and SHPB testing. We refer to such phases as "ambient" phases and the rest as "non-ambient". Because of the difficulty of measuring stress-strain curves in non-ambient phases, the multiphase model framework allows a simple description of their strength as a scaled value of the strength model in an ambient phase [19]. The scalar scale factor can potentially be calibrated by simulating high-pressure experiments that are sensitive to strength but do not give explicit calibration data like a stress-strain curve. This pragmatic approach gives some experimental basis for the model but makes simplifying assumptions about hardening and rate- and temperature-dependence that should be unique to each phase. On the other hand, an arbitrarily complex model of non-ambient phase strength is also allowed in CMMP as needed, assuming one can be constructed.

Preliminary versions of the CMMP calibration presented here were used to model the strength of polycrystalline tin across phase boundaries [12], [19]. [7] used a framework similar to CMMP, albeit with different constitutive ingredients including a combined multi-phase Birch-Murnagahan equation of state and Steinberg-Guinan [23] strength model to simulate the longitudinal wave speed [28] and the free surface velocity from plate impact experiments that crossed the β-γ phase boundary in tin [6].

Here, we calibrate a shear modulus model for most solid phases of tin using density functional theory (DFT) calculations. (The low temperature α phase is excluded because it has little practical interest and is unlikely to show up in experiments [1]). The modulus model is then validated on ultrasonic sound speed measurements. We

---

[1] Although the title has changed, this paper is the "in preparation" reference 42 in [19].

then calibrate a temperature, plastic strain, and plastic-strain-rate dependent strength model for the ambient β phase using QS and SHPB testing over a broad range of temperatures and strain rates. Finally, to validate the model, both traditional (i.e. forward) and reverse Taylor anvil impact experiments were performed. The significant temperature rise associated with the large deformation of the Taylor impact tests leads to localized melting, thus testing the multiphase model because of the solid-liquid phase change and regions of mixed solid and liquid phases.

2. Experimental Methodology

This section discusses the experimental techniques used to characterize tin, measure its mechanical behavior and the Taylor anvil experiments.

2.1. Source material

The tin material used in this investigation is 99.8% pure and was obtained from Vulcan industries in plate form. The plate was uni-axially cold-rolled and then annealed at a low temperature. The chemistry for this material is shown in Table 1.

Element	Amount (wt %)
Tin	99.82
Oxygen	0.0025
Nitrogen	< 0.0005
Carbon	0.0019
Sulfur	< 0.0005
Lead	0.11
Copper	0.054
Indium	0.0099

Table 1: Chemical composition of the tin plate.

The microstructure of the plate was characterized in the through-thickness direction and the two in-plane directions (including the rolling direction) using electron back scatter diffraction (EBSD). Each specimen was prepared for microscopy using standard metallographic techniques. Sample preparation consisted of grinding on SiC paper with increasingly fine grit under very light pressure, followed by mechanical polishing with 0.3 μm alpha alumina slurry, and then a mixture of 10:1 by volume of 0.04 μm colloidal silica and hydrogen peroxide. The polished sample surfaces were etched with a solution containing 9 ml hydrochloric acid, 3 ml nitric acid, and 10 ml water. A Zeiss Axio Imager M2m optical microscope was used to interrogate the etched surface and to identify regions of interest for electron microscopy. Electron Backscatter Diffraction (EBSD) was employed to investigate the cross sections of the samples on a Thermo Scientific$^{\text{TM}}$ Apreo SEM, using the EDAX OIM Analysis$^{\text{TM}}$ Data Collection and Analysis software. EBSD data was acquired with a step size of 1 μm for texture measurements, as well as with a step size of 0.5 μm to obtain detailed information on the spatially varying microstructure.

These EBSD micrographs along the different directions are shown in Fig. 1. This figure shows that there is a slight difference in grain size as a function of orientation. Specifically, the grain size is ∼80 μm in the through-thickness direction and 82 and 87 μm in the two in-plane (IP) directions. There is also variation in the texture as a function of orientation. The texture is slightly (001) in the TT direction and the rolling direction (RD) as compared to the (110) texture in the transverse direction. This is mild texture typical of rolling. In the mechanical testing we measure stress-strain curves in orthogonal directions to see if there is any plastic anisotropy due to this difference in texture.

2.2. Mechanical behavior

Cylindrical samples were electro-discharge machined from the through-thickness (the compression axis was parallel to the plate through-thickness direction) and two in-plane orientations (parallel to the rolling direction and orthogonal to the rolling direction) to dimensions of 5 mm in height and 5 mm in diameter for quasi-static and dynamic mechanical testing. The quasi-static (QS) compression experiments were conducted using an Instron screw-driven test system at strain rates of 0.001, 0.1, and 5.0 s^{-1} and temperatures ranging from 87 to 373 K, with MoSi2 lubrication on the interfaces to minimize barreling. Dynamic compression testing was conducted using a split-Hopkinson Pressure Bar (SHPB). The SHPB samples were similarly lubricated using MoSi2 to minimize friction at the sample-pressure bar interfaces. Data was collected at temperatures ranging from 193 to 373 K at strain rates of approximately 3×10^3 s^{-1}. The specifics of each loading condition are shown in subsection 3.1 with the results.

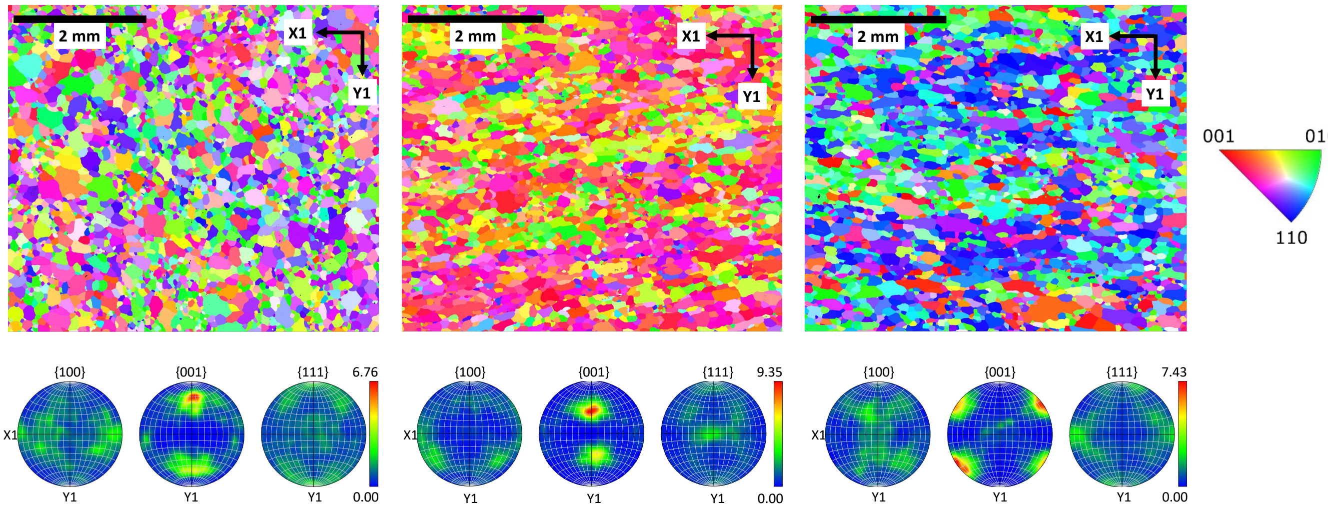

(a) Through-thickness direction (TT) (b) Rolling direction (RD) (c) In-plane direction (IP)

Fig. 1: EBSD micrographs, texture analysis, and grain size distribution along the through-thickness (TT), rolling (RD) and in-plane (IP) directions from the material sample.

2.3. Ultrasound measurements of shear modulus

Two separate time-of-flight ultrasound experiments were performed to determine the shear modulus as a function of temperature and pressure, respectively. In both experiments, time-of-flights were measured using tone bursts over a range of carrier frequencies as described in [29, 30] to account for extraneous delays due to the medium coupling the ultrasound transducers to the sample. The high-pressure experiments were performed at High-Pressure Collaborative Access Team (HPCAT), beamline 16 BM-B (Advanced Photon Source, Argonne National Laboratory), while the high-temperature experiments were performed at Dynamic Experiments Division facilities of the Los Alamos National Laboratory (LANL).

The high-pressure experiment utilized a right circular cylindrical sample of diameter 1.50 mm and a nominal height of 0.625 mm. In the ambient-pressure, high-temperature experiments, shear wave speeds were measured in a parallelepiped sample of dimensions 4.1 x 5.1 x 6.1 mm^3. The setup used two ultrasound transducers configured in a transmit-receive geometry (as in [31]) with the wave speeds being measured along the 4.1 mm dimension. Though less common than the single transducer pulse-echo geometry, the transmit-receive geometry affords a significantly higher signal-to-noise ratio which is advantageous for highly attenuating materials such as tin. The transducer-sample-transducer assembly was placed in a temperature-controlled water bath with wave speed measurements being collected at 278 K intervals between 298 and 349 K.

Time-of-flight measurements were combined with sample dimensions to determine the velocities of the longitudinally- and shear-polarized waves. Sample dimensions were determined with X-ray radiography for the high pressure experiments and by direct measurement, accounting for thermal expansion, for the high temperature experiments. Sound velocities were combined with mass density of the sample to determine the compressional (C_{11}), shear (G), and bulk (B) moduli of the sample. For the high pressure experiments, mass density was determined by measurements of the lattice volume using X-ray diffraction. For the high temperature experiments, sample mass and volume were measured directly at ambient conditions and corrected for thermal expansion at the higher temperatures.

2.4. Forward Taylor cylinder Impact

In a traditional Taylor anvil impact experiment, a cylindrical specimen of the material of interest is accelerated along the barrel of a gas gun and it then impacts a stationary and (quasi-)rigid anvil. The specimen dimensions are typically 7.5 to 12.5 mm diameter and 25 to 40 mm in length. By tuning the impact velocities and the ratio between cylinder length and diameter, a strain rate between $10^4 - 10^6$ s^{-1} can be achieved within the specimen near the impact face. Specimens typically undergo significant and nonuniform plastic deformation across a wide range of strain rates and temperatures as the material is further heated by inelastic work. In addition to probing such a broad range of material state conditions (i.e. rate, temperature), these experiments are relatively simple and inexpensive in the context of other platforms. For these reasons, Taylor anvil impact experiments are appealing for assessing rate-dependent constitutive models under conditions of large deformation [32–34], or validating the calibrated material models [35–37].

PLEASE CITE THIS ARTICLE AS DOI: 10.1063/5.0207405

The experiments in this work were performed at the LANL Taylor cylinder facility, which uses a 30-caliber 7.62 mm (i.e. 0.300 inch) smooth-bore launch tube. It was designed to utilize high-pressure helium-gas propulsion of the cylinders rather than propellant drive. The helium gas breech and valve design is capable of consistently launching, with high repeatability, a 25-gram steel cylinder to 400 m/s using helium gas at just over 30 MPa (4500 psi). The Taylor cylinder facility launches the specimens against a pneumatically-positioned AF1410 high-strength steel anvil (polished to a mirror surface finish) contained within an evacuated thick-walled 304 stainless steel tank. All testing is conducted under vacuum conditions (typically 10 torr). The velocity of the projectile is measured using up to four laser beam timing circuits. They are positioned between the muzzle of the barrel and the impact anvil so that the beams intersect the path of the Taylor cylinder in flight.

In the experiments performed as part of this research, a specimen size of 38.2 mm length and 7.6 mm diameter was used for all (forward and reverse, cf. below) shots. The specimen velocities for the forward Taylor anvil shots, measured immediately prior to impact, were 96.1, 110.7, 116.2, 131.8, 141.1, and 153.1 m/s, respectively.

2.5. Reverse Taylor cylinder impact

In addition to the traditional (forward) Taylor anvil impact experiments, reverse Taylor impact experiments were also performed on tin. In these experiments, instead of firing a specimen onto an anvil, the opposite is done and the gas gun is used to launch an anvil at a stationary specimen, as shown in Fig. 2. One advantage of the reverse Taylor configuration is that specimens can be heated to much higher, controlled temperatures in comparison to the traditional Taylor Anvil tests. If performed correctly, these experiments are substantially equivalent to the traditional forward configuration [38]. As part of the current work, a 4340 steel anvil was mounted on the leading face of a projectile, which was then fired into cylindrical tin specimens mounted in the target tank of a 100 mm bore vertical gas-gun at LANL. The steel anvil was a right cylinder with 6.35 mm thickness and 63.50 mm diameter.

The tin specimens were mounted in a tilt ring, which was adjusted to ensure that the sample was concentric and coaxial to the gun barrel axis. A combination of a rigid steel plate and aluminum honeycomb was used to arrest the tilt ring and projectile, allowing only the tin specimen to pass through into the soft-recovery chamber of the gun, for post-mortem analyses of the shape of the Taylor cylinders. The anvil velocities measured immediately prior to impact for the reverse Taylor impact experiments in this work were 115.0 and 131.0 m/s.

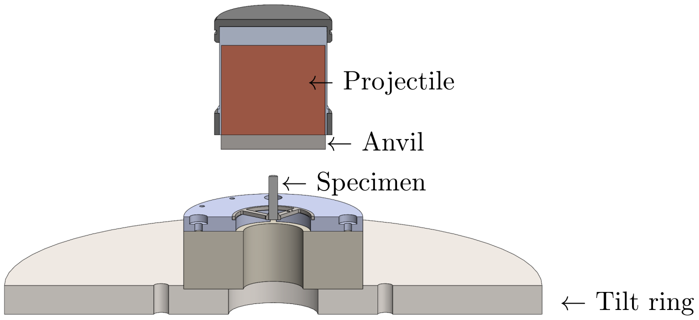

Fig. 2: Schematic of the reverse Taylor impact test on a cross section view. The size of the projectile and the anvil is not to scale.

3. Experimental Results

3.1. Mechanical behavior

Comparison of the quasi-static true stress-true strain behavior of two samples each from the through-thickness and two in-plane orientations in Fig. 3 revealed nearly identical mechanical behavior, thus eliminating concerns of anisotropic constitutive behavior. Accordingly, the remaining mechanical characterization experiments exclusively used samples sectioned and loaded in the through-thickness orientation.

Fig. 4 presents the true stress and true strain data obtained at increasing quasi-static rates (a-c) and at high strain rates (d). The data for these plots is given in the in the Supplemental Material [39]. The conditions span a broad range of temperature (87 K $< T <$ 373 K), strain rate (10^{-3} s^{-1} $< \dot{\epsilon}_{\mathrm{p}} < 4 \times 10^{3}$ s^{-1}), and sufficiently high magnitudes of strain to exhibit saturation of the flow stress under most conditions. Consistent with most ductile polycrystalline metals, the measured flow stress of $\beta-$tin is significantly dependent on the strain rate and temperature. Specifically, decreasing the temperature and/or increasing the strain rate leads to an increase in the magnitude of the flow stress. At room temperature ($T = 293$ K), the flow stress at low strain increased from 12 MPa at a strain rate of 10^{-3} s^{-1} to 40 MPa at a rate of 10^{3} s^{-1}. This pronounced rate dependence is consistent with the known behavior of lower symmetry metals and alloys with a high Peierls barrier to dislocation motion.

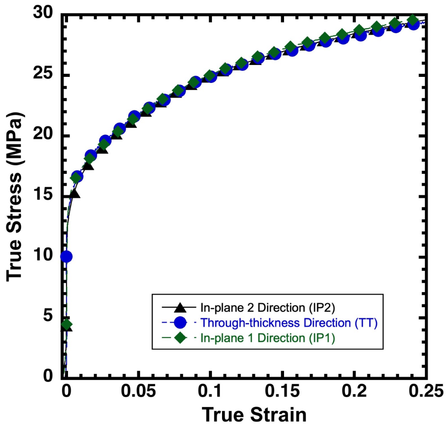

Fig. 3: True Stress-true strain data corresponding to the different directions of the plate shows no significant anisotropy.

At higher strain rates, the work hardening behavior displays a sigmoidal shape, i.e., an early concave upward steep increase in the work-hardening rate before rolling over to saturate at higher plastic strains. This observation also applies to the coldest QS experiment at $T = 87$ K. This feature in the mechanical response may be attributed to the nucleation and growth of deformation twins. EBSD was not performed on the compression samples to quantify twin volume fraction, partly because the plastic work heating would likely lead to recrystallization of the recovered samples before twins could be observed. However, such a transition in the dominant mechanism accommodating the deformation from dislocation-based slip to twin activation (which is associated with the sigmoidal shape) is widely recognized and documented for other crystalline metals [40–43].

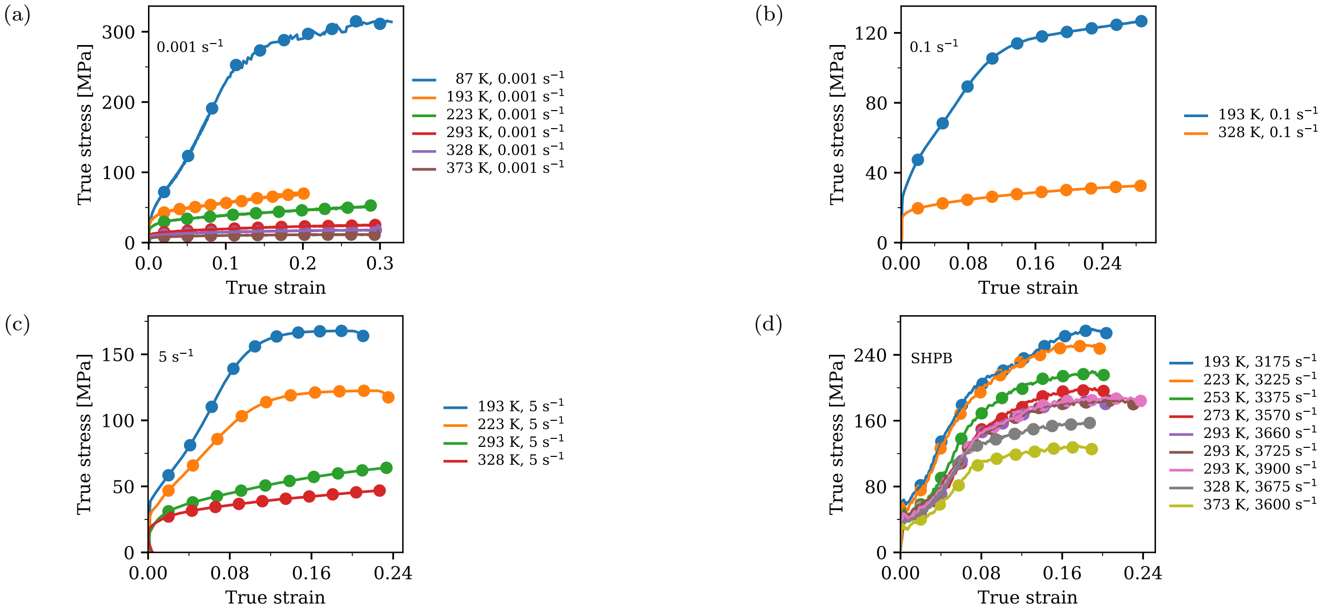

Fig. 4: True stress and true strain data from QS (a-c) and SHPB (d) experiments with conditions spanning a broad range of temperature (87K $< T <$ 373K) and strain rate (10^{-3} s$^{-1} < \dot{\epsilon}_p < 10^4$ s^{-1}). The markers correspond to stress and strain pairs used within the Bayesian calibration procedure.

3.2. Forward and reverse Taylor impact

Following both the forward and reverse Taylor anvil impact experiments, the dimensions (i.e. length, diameter) and external surface profile of each specimen were carefully measured with calipers and also photographed to enable direct comparison with simulation results (cf. Fig. 5). The cylinder impacted at 153.1 m/s experienced local failure at the footprint and the one impacted at 141.1 m/s showed some signs of incipient failure at the footprint. Key deformed dimensions for the forward and reverse Taylor anvil experiments are listed in Table 2.

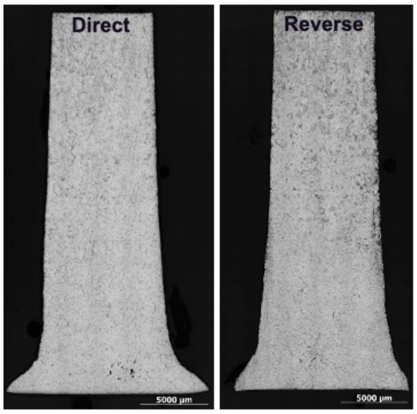

Fig. 5: Deformed cylinders after forward (direct) impact experiment (left) and reverse impact experiment (right). The impact velocity values are 131.8 m/s and 131.0 m/s on the forward and reverse impact experiment, respectively.

In addition to measuring shape changes, each of the Taylor cylinders was also sectioned across longitudinal axis to allow for quantitative metallographic and EBSD study of the cross-section to understand deformation mechanisms along the length of the cylinder. Results for the 131.8 m/s cylinder are shown in Fig. 6(a). With only modest changes at different impact velocities, the microstructure observed in Fig. 6(a) within each specimen varied along the specimen length and exhibits four distinct regions starting from the impact end: (i) small grains from recrystallization due to heating after impact, (ii) more modestly refined grain size from more modest heating, (iii) in addition to deformed grains occasional twinning is observed (not in this example), and finally (iv) deformation twins in addition to dislocation slip activity in the far region that experienced modest plastic deformation and heating. We did not measure the twin size in our deformed specimens. At the higher impact velocities, the refined grain size near the impact surface decreases, as shown in Fig. 6(b). Since tin has a low melting temperature (∼ 500 K at ambient pressure), the adiabatic heating associated with large plastic deformation at high strain rate would likely result in recrystallization of the grains and remove any evidence of twinning. The microstructures of the deformed sample in Fig. 6(a) are consistent with the level of applied strain, and accompany heating, from the impact. In particular, the applied strain increases from the cylinder free end (iv), with visible deformation twins, to the impact surface (i), with substantial reduction of grain size due to recrystallization.

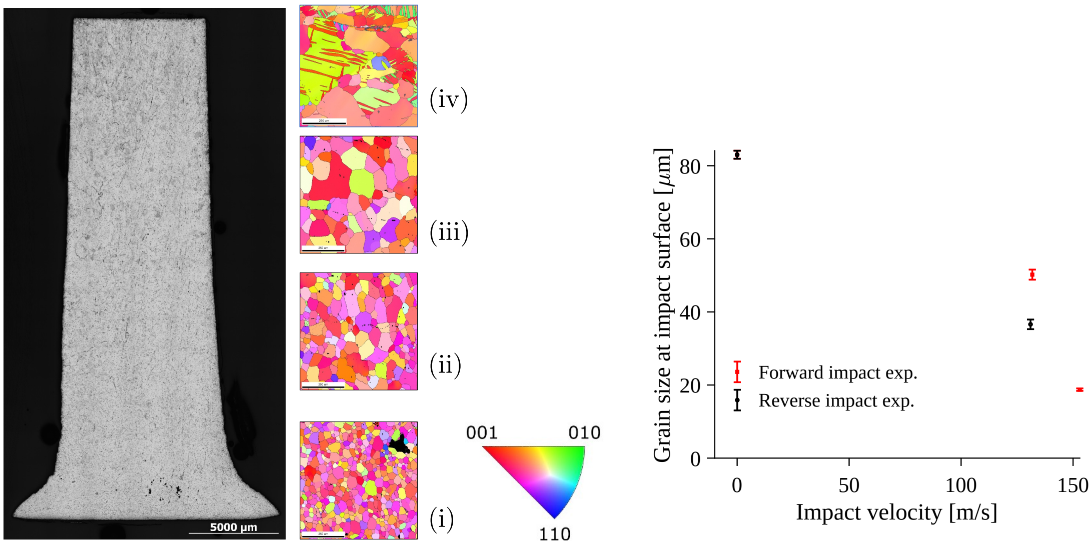

(a)

(b)

Fig. 6: (a) Microstructures (right) of the Taylor cylinder specimen (left) after forward impact test at 131.8 m/s, along the impact direction and (b) average grain size at the impact surface as a function of impact velocity indicate some recrystallization where plastic work raised the temperature. Error bars are the standard error of the mean.

3.3. Shear modulus

Fig. 7 shows the response of the β-phase elastic moduli to changes in temperature (Fig. 7(a)) and pressure (Fig. 7(b)). The uncertainty is dominated by our ability to measure the time-of-flight. Factoring that in, the es-

Journal of Applied Physics

AIP Publishing

PLEASE CITE THIS ARTICLE AS DOI: 10.1063/5.0207405

Impact manner	Impact velocity (m/s)	Exp. deformed length (mm)	Exp. deformed foot diameter (mm)
Forward	96.1	31.480	9.750
Forward	110.7	30.270	12.043
Forward	116.2	29.340	12.037
Forward	131.8	28.150	15.130
Forward	141.1	27.055	17.351
Forward	153.1	25.440	21.033*
Reverse	115.0	29.13	12.78
Reverse	131.0	28.47	12.71

Table 2: Deformed dimensions of each polycrystalline tin cylinder from forward and reverse Taylor impact experiments. Diameter measurement denoted with * is estimated from the remaining part of the foot.

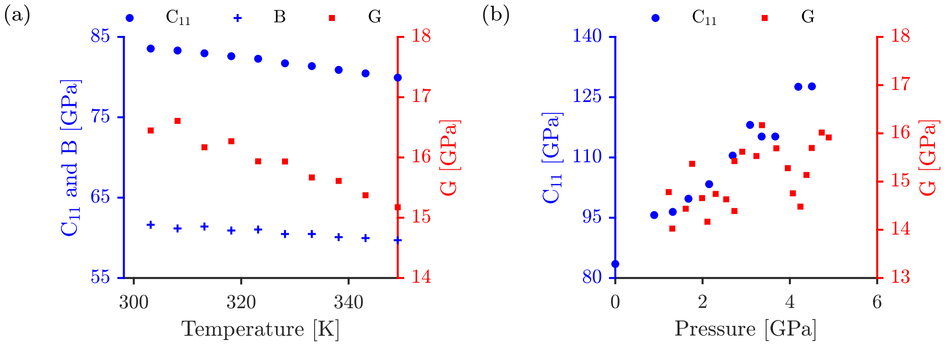

Fig. 7: (a) Compressional modulus, C_{11}, bulk modulus (B), and shear modulus (G) as a function of temperature at ambient pressure. (b) The pressure dependence of the compressional modulus, C_{11} and G up to 5 GPa at ambient temperature.

timated uncertainty in G for the smaller specimens of Fig. 7(b) is about 10% compared to only about 1% for Fig. 7(a). As is common with most materials, the elastic moduli soften with increasing temperature and stiffen with increasing pressure. Overall, the measured shear modulus in Fig. 7(a) is consistent with [44], and slightly lower than [45] (data comparison is presented in subsection 4.1). From Fig. 7(b), it can be seen that the shear modulus is much less sensitive to changes in pressure than the compressional modulus, with G increasing by only $\sim$ 15% over the 5 GPa pressure range while C_{11} increases by roughly 50%. The G values in Fig. 7(b) mostly range between 14 and 16 GPa, and the trend extrapolates back to a value of about 14 GPa at ambient pressure, which is about 17% lower than the ambient value of 16.9 GPa from Fig. 7(a). The samples for the G(P) measurements were significantly smaller than those used in the G(T) measurements. With smaller samples, the plane wave approximation (which assumes a laterally infinite sample) becomes increasingly more approximate. Wave guiding due to the edge effects can become more significant and this will serve to slow the wave. This potential bias is consistent with lower values in Fig. 7(b).

4. Multi-phase Strength Model

In this work, we use the CMMP multi-phase strength, equation-of-state (EOS), and kinetics model [19] described in the Introduction. This section describes the parameterization of the shear moduli and melt temperatures for the solid phases of tin. It then provides details of the constitutive model parameterization for β-phase tin.

The parameterizations in this section pair with a specific EOS, which gives the phase boundaries and relates the thermodynamic state variables of pressure, density, temperature, and internal energy within each phase. For an example of the coupling, the EOS determines the conversion of plastic work energy to temperature (i.e., the specific heat), which ultimately affects the strength.

The need for a melt temperature model may not be obvious. After all, the EOS gives the solid liquid phase boundaries and is used to determine the fraction of liquid at any point during a calculation. The analytic parameterization of the melt temperature is used more indirectly. In this work, both the shear modulus model and the constitutive model use the homologous temperature, the ratio of the temperature relative to the material's melting temperature, as a key physical parameter. The melt temperature is thus needed for each solid phase. However, since some phases do not melt directly without first transforming to another solid phase, there is no phase-specific melt temperature available from the EOS. Thus, an analytic treatment is used, even though the melt temperature may in some sense be virtual or a reference ([19]).

There is also a special consideration for the shear modulus model. With phase change kinetics, a solid phase can exist outside its equilibrium boundaries. To evaluate the contribution to strength in such a state, a finite, positive shear modulus is required not only within in each equilibrium phase region but to some extent beyond the boundaries. The shear modulus model should be checked against the EOS to ensure this is the case.

Equations of state for tin have been constructed using experimental data [6–8], density functional theory [1, 46], and molecular dynamics [47]. The parameterizations here use the SESAME 2162 multiphase EOS for tin [1], which was constructed using density functional theory and extensive comparisons to isobaric data, isothermal data, shock data, and phase boundary measurements. SESAME 2162 was specifically constructed as a set of individual phase tables to be employed within a model like CMMP.

Since our work here began, SESAME 2162 was updated to 2163 [20] to account for more recent experimental data. The β-γ phase boundary was moved slightly higher in pressure, to better align with recent measurements [48]. The melt curve at pressures greater than 50 GPa (well above the β phase) was adjusted to match data [49–51]. Adjustments were also made to the higher pressure δ and ϵ phases and the γ-δ phase boundary. Because changes to the β phase were minimal, simulations of the experiments in this work using the parameterizations for 2162 (i.e. uniaxial stress compression and Taylor cylinder impact experiments) will be repeated using 2163 to see if the results change.

Hydrocode simulations are used for two purposes in this work. First, fitting the constitutive model to the experimental data is done using hydrocode simulations. Using a simulation instead of an analytic evaluation of the constitutive model ensures that the fit is consistent with the EOS being used. Second, the Taylor cylinders are simulated using the fully calibrated CMMP model for validation purposes. The experiments were modelled using FLAG, an arbitrary Lagrangian/Eulerian, explicit, finite-volume hydrocode using arbitrary polyhedral computational zones [52].

The multiphase aspect of the strength model is tested by the Taylor cylinders because the simulations for higher impact velocities reach the melt temperature in the highest deformation regions. The CMMP model allows smooth transitioning from full strength solid to a mixed solid-liquid state with reduced strength. CMMP is also compared with simpler approaches with an abrupt transition to liquid. Testing CMMP on experiments which undergo solid-solid phase transformations is left for future work.

4.1. Shear modulus model

We use the Preston-Wallace (PW) model [24] to describe the variation of shear modulus with respect to density and temperature, within each solid phase of tin, i.e.

$$G\left(\rho,T\right)=G_0\left(\rho\right)\left[1-\alpha\frac{T}{T_m\left(\rho\right)}\right] \tag{1}$$

where $G_0\left(\rho\right)$ is referred to as the cold shear modulus, $T_m\left(\rho\right)$ is the melt temperature of the material corresponding to a particular density, and α is a material parameter that reproduces the observed linear variation of shear modulus with respect to temperature (at fixed density) for most metals over a range of temperatures away from $T=0$. Note that (1) the cold shear modulus is somewhat of a misnomer because Eq. (1) does not hold for temperatures approaching $T=0$. And (2) the melt temperature $T_m\left(\rho\right)$ is, in some sense, a virtual melt temperature because the material may not be able to melt from a given solid phase without first undergoing a solid-to-solid phase transformation and the associated change in density. The Burakovsky-Greeff-Preston model is based on the Lindemann criterion [26], i.e.,

$$\frac{d\ln T_m}{d\ln\rho}=2\left(\gamma\left(\rho\right)-\frac{1}{3}\right) \tag{2}$$

where the Grüneisen parameter is assumed to vary with density according to

$$\gamma(\rho)=\frac{1}{2}+\frac{\gamma_1}{\rho^{1/3}}+\frac{\gamma_2}{\rho^q}, \tag{3}$$

and the dislocation-mediated melting model [53] in which the relation $\frac{G(\rho,T_m(\rho))}{\rho\cdot T_m(\rho)}=\text{const}$ [54] provides a direct connection between $G_0(\rho)$ and $T_m(\rho)$, in view of Eq. (1) in which α is assumed to be density independent. The way we derived the numerical values of the parameters γ_1, γ_2 and q is described in detail in [26].

While the original model developed by [26] results in a similar expression for the cold shear modulus using the same expression for the Grüneisen parameter as in the melt temperature, in practice it has been effective to employ a parameterization similar to Eq. (2) and Eq. (3) pertaining to the cold shear modulus and the melting temperature separately, i.e. [27],

$$\frac{d\ln G}{d\ln\rho}=2\gamma_G(\rho)+\frac{1}{3},\quad \frac{d\ln T_m}{d\ln\rho}=2\gamma_{T_m}(\rho)-\frac{2}{3}, \tag{4}$$

phase	ρ_{ref} g cm^{-3}	G_{ref} GPa	ρ_{m} g cm^{-3}	T_{ref} K	γ_1 g$^{1/3}$ cm^{-1}	γ_2 $(\text{g cm}^{-3})^{q_2}$	q_2 -	γ_3 $(\text{g cm}^{-3})^{q_3}$	q_3 -	α -
β	7.40	25.4	7.180	505.1	0.000	600	3.2	800	3.2	0.53
γ	7.82	26.8	7.585	595.0	0.000	820	3.2	2300	3.2	0.7
δ	10.50	23.0	9.425	1900	2.125	5.5×10^8	8.0	1.1×10^8	8.0	0.2
ϵ	10.30	44.5	9.950	2455	2.170	1.4×10^7	8.0	1.1×10^8	8.0	0.4

Table 3: Parameters for phase-specific melt temperature and shear modulus models for tin.

with

$$\gamma_G(\rho) = \frac{1}{2} + \frac{\gamma_1}{\rho^{1/3}} + \frac{\gamma_2}{\rho^{q_2}}, \quad \gamma_{T_m}(\rho) = \frac{1}{2} + \frac{\gamma_1}{\rho^{1/3}} + \frac{\gamma_3}{\rho^{q_3}}. \tag{5}$$

That is, $G(\rho, 0)$ and $T_m(\rho)$ are described by separate sets of parameters $(\gamma_1, \gamma_2, q_2)$ and $(\gamma_1, \gamma_3, q_3)$, respectively, with γ_1 being the only common parameter for both sets. The theoretical value of γ_1 is [27] $\gamma_1 = \frac{7}{40} \cdot Z^{2/3}$, where Z is the atomic charge. In a general case, the value of γ_1 should be close to $\frac{7}{40} \cdot Z^{2/3}$ but not necessarily equal to it.

The solution of Eq. (4) and Eq. (5) leads to the expressions for the variation of melt temperature and cold shear modulus with density, i.e.,

$$G_0(\rho) = G_{\text{ref}} \left(\frac{\rho}{\rho_{\text{ref}}}\right)^{4/3} \exp\left[6\gamma_1 \left(\frac{1}{\rho_{\text{ref}}^{1/3}} - \frac{1}{\rho^{1/3}}\right) + \frac{2\gamma_2}{q_2}\left(\frac{1}{\rho_{\text{ref}}^{q_2}} - \frac{1}{\rho^{q_2}}\right)\right] \tag{6}$$

$$T_m(\rho) = T_{m,\text{ref}} \left(\frac{\rho}{\rho_{\text{ref}}}\right)^{1/3} \exp\left[6\gamma_1 \left(\frac{1}{\rho_{\text{ref}}^{1/3}} - \frac{1}{\rho^{1/3}}\right) + \frac{2\gamma_3}{q_3}\left(\frac{1}{\rho_{\text{ref}}^{q_3}} - \frac{1}{\rho^{q_3}}\right)\right] \tag{7}$$

Together, Eq. (1), Eq. (6) and Eq. (7) constitute a complete analytical model for the shear modulus and melt temperature across a range of density and temperature.

Fig. 8 compares the results of the ab initio calculations on the cold shear moduli of four different solid phases of tin using the Vienna Ab initio Simulation Package VASP to the model envelope for which the input parameters are those of β-tin that are given in the first four columns of Table 3. The use of $\gamma_G(7.40) = 1.36$ based on the results of [48] leads to the following set of the model parameters for the $G_0(\rho)$ envelope: (for tin $Z = 50$) $\gamma_1 = \frac{7}{40} \cdot 50^{2/3} = 2.37512$, $\gamma_2 = -1.2$, $q_2 = 0.6$.

Now we further modify this generalized model to make it applicable to each of the solid phases of a multi-phase material separately to make the description of each phase more accurate. The modification consists of introducing separate sets of parameters for each of the solid phase of a multi-phase material assuming the validity of the basic relations given in Eq. (1), Eq. (6) and Eq. (7) phase-by-phase. The δ and ϵ phases do not have well established or agreed upon existence limits at high pressure, and are thus treated similar to the general case. The $P \to \infty$ asymptotic conditions on $G_0(\rho)$ and $T_m(\rho)$ used for the calculation of the model parameters [27] are applied. The entire parameter sets, including the corresponding values of γ_1 are obtained using the scheme of [27] and are also shown in Table 3.

The β and γ phases are stable only in a finite pressure range and must be treated differently. The $P \to \infty$ asymptotic conditions are dropped. In this case, the number of constraints on the model parameters as given in [27] may not be enough to obtain the values of all of the needed values. In this case, one can still reliably describe a given solid phase of a multi-phase material with a lesser number of model parameters. Eliminating γ_2 would eliminate q_2, as well since the entire second term in Eq. (5) is gone. In practice, it is better to eliminate γ_1 while keeping both γ_2 and q_2 (and, respectively, both γ_3 and q_3 for T_m) since γ_1 is directly related to the $P \to \infty$ behavior of both G and T_m, which is irrelevant for phases that exist in a limited pressure range. The remaining values are then calculated using the scheme developed in [27] and are shown in Table 3.

The values of α for all four phases are calculated based on the linear fits of the form given in Eq. (1) to the results of VASP simulations on G at finite T. Fig. 9 illustrates such simulations for β-tin. The corresponding value of $\alpha = 0.53$ comes from averaging the values of the slopes of linear fits at three different densities. For another three solid phases of tin, the results on $G(\rho, T)$ are such that the values of linear slopes are not as close to each other as those in the case of β-tin, so that the other three values of α are rounded to the first principal digit (cf. Table 3).

Using Eq. (1) with $G_0(\rho)$ and $T_m(\rho)$ defined in Eq. (6) and Eq. (7), respectively, one can calculate $G(T, \rho)$ for every solid phase of tin using the corresponding parameter values from Table 3. Specifically, using a collection of densities that correspond to $P = 0$ at different temperatures (they can be obtained using SESAME 2162), one can calculate the T-dependence of G at ambient P. Such T-dependence of G for β-tin is shown in Fig. 10 and compared to our own

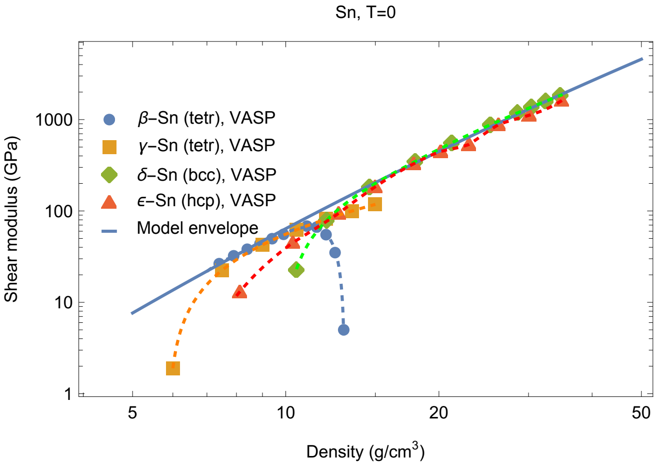

Fig. 8: Cold shear modulus as a function of density: comparison of Eq. (6) (model envelope) to the ab initio results on four solid phases of tin obtained using the VASP software which are shown with different symbols. Dashed lines are added as a guide to following the individual phase points.

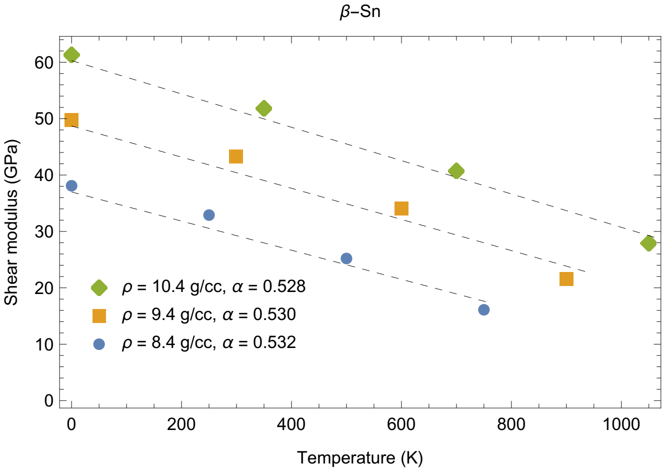

Fig. 9: Shear modulus of β-tin as a function of T at three different densities. Dashed lines represent the best fits of the form given in Eq. (1) to the corresponding ab initio data computed using the VASP software.

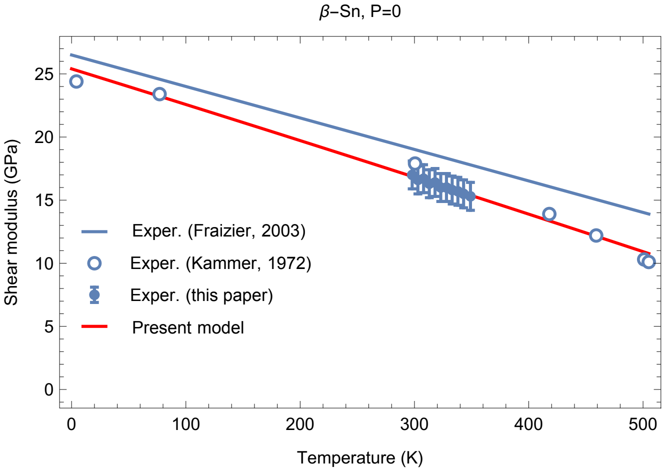

Fig. 10: The T-dependence of G at $P = 0$ for β-tin: our theoretical model (Present model) versus our own experimental results (this paper) as well as those of [44] and [45].

experimental results from Fig. 7(a) as well as earlier experimental data [44] and [45]. It is clear that the agreement between the model and experiment is excellent except the data by Fraizier et al. [45] which give somewhat higher values of G and weaker T-dependence.

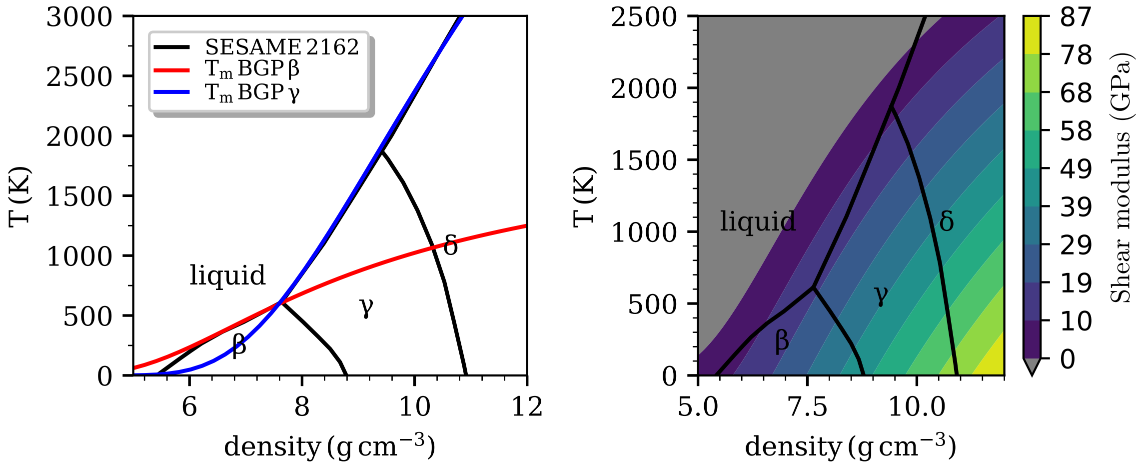

(a) Equilibrium phase diagram

(b) $G_\beta\,(\rho, T)$

Fig. 11: (a) The phase-specific reference melt temperatures from Eq. (7) and parameters in Table 3 coincide well with the boundaries between solid and liquid phases according to the multi-phase equation of state, SESAME 2162 [1]. (b) Shear modulus model values for the β phase. The shear modulus needs to be defined outside the equilibrium phase boundaries so that strength can be evaluated when phase change kinetics allows phases to exist there.

Unfortunately, the G vs. P data in Fig. 7(b) does not help validate the model. First, the magnitudes of the G values are affected by the apparent bias in the data discussed in subsection 3.3. Second, the scatter in Fig. 7(b) over the relatively small range of pressures results in no meaningful constraint on the slope.

Fig. 11 illustrates the final phase-specific shear modulus model and parameters. Fig. 11(a) shows that the 'reference' melt temperature for the β and γ phases agree well with with the equilibrium phase boundaries from SESAME 2162. Fig. 11(b) shows that the value of the β-phase shear modulus is defined well beyond its equilibrium existence region. The shear moduli need to be defined outside their equilibrium phase boundaries, including possibly into the liquid, so that strength can be evaluated when phase change kinetics allows phases to exist there.

4.2. Parameterization of the Preston-Tonks-Wallace strength model for the β phase

This accurate shear modulus model is combined with a viscoplastic model to capture thermomechanical response of tin during dynamic deformation. Popular viscoplasticity models for polycrystalline metals include the Johnson−Cook empirical model [55], mechanical threshold stress (MTS) [56, 57], and the Preston-Tonks-Wallace (PTW) model [25]. In these models, the flow stress is modeled as a function of strain, strain rate, temperature, and sometimes pressure or density. Among the above models, PTW is the only constitutive model in which the flow stress at thermal-activation regime is smoothly transitioned into that of the over-driven shock regime [58, 59]. This feature makes the PTW model applicable for a wider range of strain rates, from quasi-static to extreme loading conditions created by high-velocity impacts [60] and a broad range of experimental platforms that reach extreme conditions [61]. The PTW model normalizes temperature by the melting temperature, and flow stress by shear modulus. These characteristics of the PTW model make it suitable for modeling polycrystalline tin, which is known for low melting temperature and strong temperature and density/pressure dependence of the viscoplastic behavior. Other physics-based models, such as the dislocation-based crystal plasticity model [62, 63], are applicable for high rate deformation of tin with proper modification to address the above thermomechanical characteristics of tin.

In this section, we calibrate the PTW model parameters against the uniaxial stress-strain data for β-phase tin obtained from the QS and SHPB compression experiments. Since the shear modulus is modeled separately from the PTW model, there are 11 remaining PTW parameters: θ, p, S_0, S_∞, Y_0, Y_∞, κ, γ, y_1, y_2, β. The three PTW parameters y_1, y_2, and β determine the material strength only at the transition strain rates from thermally activated regime to over-driven shock regime and higher rates. They are not sensitive to the uniaxial stress measurements at SHPB loading rate and lower. Therefore, the three parameters are held constant at $y_1 = 0.0355$, $y_2 = 0.45$, and $\beta = 0.45$. These values come from unpublished internal work based on limited information and should be treated with caution in applications where simulation results are sensitive to these parameter values.

Bayesian model calibration (BMC) was performed using the Sepia package [64] to calibrate eight PTW parameters: θ, p, S_0, S_∞, Y_0, Y_∞, κ, γ. Previously, BMC was used to calibrate the Johnson-Cook model on Al [65] and a single crystal plasticity model for copper [66] and tantalum [37]. Our approach to calibrate the tin PTW model parameters closely follows those works. The approach consists of the four following steps,

- Sampling a non-informative uniform *prior* distribution of the parameters over some pre-selected ranges.

Parameter	Lower limit	Upper limit	Expected value
θ	0.02	0.12	5.97E-2
p	1E-04	6.00	2.82
S_0	0.012	0.035	2.56E-2
S_∞/S_0	0.01	0.04	2.63E-2
Y_0/S_0	0.04	0.25	9.32E-2
Y_∞/S_∞	0.01	1.00	0.46
κ	0.12	0.24	1.86E-1
$\log_{10}(\gamma)$	-6.5	-5.5	-5.87

Table 4: The PTW model parameters' calibration ranges and expected values. The expected values comprise the fit designated as sn06.

- Modeling the corresponding responses of the physical computational model using the sampled parameter sets and extracting the measurements equivalent to the experiment observations.
- Training the Bayesian emulator with the parameter inputs and simulation outputs to provide simulation outputs of any parameter inputs without invoking the physical computational model and cross validating the emulator performance.
- Drawing Markov Chain Monte Carlo (MCMC) realizations of the *posterior* parameter distribution, which brings the simulated response into agreement with the experiment observations.

The calibrated parameter ranges of eight parameters are given in Table 4. 400 parameter sets are sampled from a non-informative uniform *prior* distribution of the parameters over the pre-selected ranges. The parameter sets are used in one-zone simulations of idealized uniaxial stress loading at constant true strain rate [37, 66]. All SHPB experiments are simulated assuming adiabatic conditions, while all quasi-static experiments are simulated assuming constant temperature. In particular, 10 stress measurements are extracted from each of 21 uniaxial stress-strain curves. The 10 stress measurements correspond to linearly spaced strain values between 0.02 and the respective maximum measured strain as shown as markers in Fig. 4. Therefore, the stress measurements represent the early yielding, material hardening and saturation behavior of each loading conditions. Corresponding stress responses are extracted from the simulation results of 400 parameter sets (light grey solid lines in Fig. 14) and used to train the Bayesian emulator.

The trained emulator is then cross-validated by holding out one pair of input (parameter set)-output (stress responses) and using the rest of input-output pairs to predict the held out output. The cross-validated value is plotted against the physical model simulated value in Fig. 12 (colored by the Gaussian kernel density estimation of the pair values). The high density toward the line of $y = x$ in Fig. 12 indicates good performance of the emulator in the given parameter ranges (cf. Table 4).

The posterior parameter distributions resulting from 480,000 MCMC draws for calibration to the uniaxial stress experiments are presented in Fig. 13. The diagonal plots present the marginal probability distributions associated with the particular parameter indicated on the horizontal or vertical axis labels. The marginal distributions are expressed as a probability density which integrates to unity. The plots below the diagonal represent the correlation between the individual parameters. The expected parameter values of each marginal distribution are presented in Table 4, and designated as fit sn06 for tracking purposes. As can be seen in the posterior distributions, the stress measurements can well constrain six parameters θ, S_0, S_{inf}, Y_0, κ, γ. The two parameters p and Y_∞, are not as well constrained in the marginal distributions. However, the correlation plots show a strong correlation of those two parameters with respect to other parameters such as $p - S_0$, $p - S_\infty$, $p - \gamma$, $Y_\infty - \theta$. Therefore, these two parameters are constrained by the uniaxial stress results in conjunction with the other parameters.

The uniaxial true stress versus true strain behavior using the prior parameter sets, posterior parameter sets and expected value parameter set are compared to the corresponding experimental measurements in Fig. 14. The simulations using prior parameter sets, plotted as light grey lines, shows that the calibration set used to train the emulator spans the domain of the experimental data. Such coverage is required to obtain a good model calibration, although this coverage does not in itself guarantee the model can simultaneously fit all the experiments.

The posterior parameter sets and expected value parameter set generally agree well with the experimental observations across the wide ranges of temperature and strain rate. The PTW model does not capture the sigmoid shape associated with twinning. Rather, it smooths through that feature and the higher strain hardening. Nonetheless, the average error between the stress measurements from simulations using the expected parameter values and experiment is 8.43 MPa. This accuracy is excellent given the wide range of loading temperature and strain rate, the large number of experiments (21), and the limitations of PTW to capture effects like twinning.

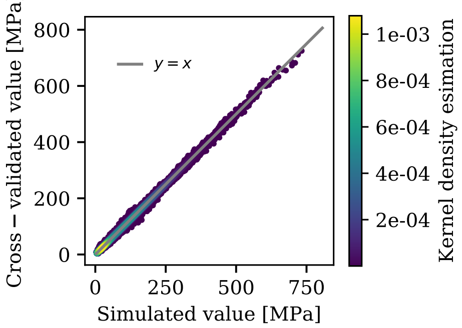

Fig. 12: The stress values predicted by the emulator from cross-validation predictions versus FLAG simulated stress values for 21 uniaxial stress loading conditions show that the emulator used for Bayesian model calibration is accurate. Each pair of values on the scattered plot is colored by the Gaussian kernel density estimation.

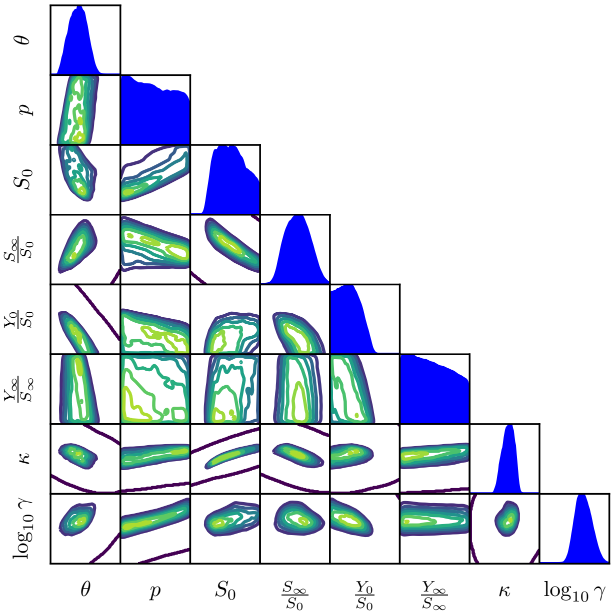

Fig. 13: Posterior parameter distribution for calibration of true stress measurements. The plots on the diagonal present the marginal distribution of each parameter. The off-diagonal plot presents the two dimensional bivariate kernel density estimation between pairs of parameters. The limit on each plot is [0 1] of the corresponding standardized range of parameter values in Table 4.

5. Validation on Taylor Cylinder Impact Experiments

In this section, we validate our calibrated strength model against the deformed shapes of Taylor cylinders from both the forward and reverse impact experiments described in section 2. For the simulations, the cylinder and anvil materials are assumed to be isotropic. In addition, their 3D structures have axial symmetry. Therefore, the 3D structures are adequately modeled with axisymmetric 2D models as shown in Fig. 15. The anvil and the cylinder are meshed with axisymmetric quadrilateral computational zones of approximately equal sizes. The steel anvil is meshed with 60 zones along the radial direction, and 12 zones along the axial direction. The tin cylinder is meshed with 144 zones along the radial direction, and 432 zones along the axial direction, resulting in an aspect ratio of 3.35. This aspect ratio has the advantage of avoiding large zonal distortion near the contact surface of the deformed cylinder, where the radial direction expands while the axial direction contracts significantly.

The initial temperature of both cylinder and anvil is $T = 300$ K. The impact simulations are modeled as adiabatic processes. The initial velocities are applied to either the cylinder (in the forward impact simulations) or the anvil (in the reverse impact simulations) by initializing the velocity on all vertices (i.e. nodes) within the corresponding meshes. In the forward Taylor simulations, the anvil is held analytically fixed. In reverse Taylor simulations, the anvil is modeled with the thermomechanical behavior of 4340 steel. Parameters for the equation of state and strength of 4340 steel were taken from [67]. The forward and reverse Taylor cylinder impact simulations continue until the tin cylinder is separated from the anvil such that significant plastic deformation has ceased.

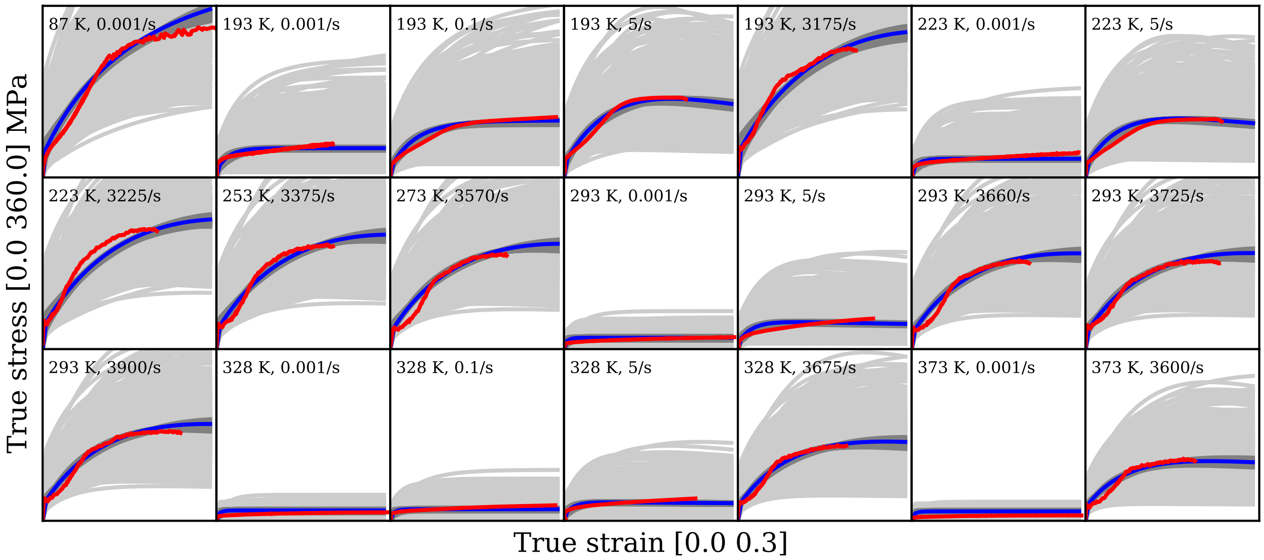

Fig. 14: Comparison of the true stress versus true strain curves between experiments (red lines) and simulations using prior parameter sets (light grey lines), posterior parameter sets (dark grey lines), and expected value parameter set (blue lines). The loading conditions of temperature and strain rate are presented in each subplot. In each subplot, the true strain is in the range of [0, 0.3] while the true stress is in the range of [0, 360] MPa.

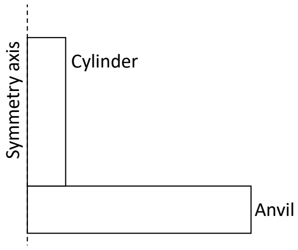

Fig. 15: Schematic of the Taylor cylinder impact tests, idealized in the two dimensional axisymmetric model.

In order to assess the potential effects of interface friction between the polished anvil and the cylinder specimen, an additional simulation of the V=153.1 m/s impact velocity case was performed with a Coulomb friction coefficient of 0.20. The simulation results for the cases with and without friction are approximately identical. Therefore, we omitted friction for the remainder of the simulation results presented in this paper. The resulting deformed shapes of the cylinders with frictionless contact boundary are used to compare with the experimental results in the following.

Fig. 16 compares the deformed cylinder shapes from the forward Taylor impact experiments with the corresponding simulations. Fig. 17 does the same for the reverse Taylor impact experiments. The model does not predict the shape well for the forward impact at 153 m/s because that cylinder had significant damage, and there was no damage model in the simulations. On all the other experiments, the simulation results show good general agreement with the corresponding measurements of the deformed profiles. Key dimensions of the deformed cylinders from experiments and simulations are presented in Table 5, and the experimental data for the deformed shapes are given in the Supplemental Material [39].

Fig. 18 summarizes the trends and model comparisons for all of the Taylor cylinders. The deformed lengths from the forward Taylor cylinders shows a smooth trend with increasing velocity that is well captured by the model, with an average error under 1%. The model predicts about 2% longer deformed length for the reverse Taylor cylinders compared to the forward cylinders at the same impact velocity, indicating less deformation of the former. This modest difference is roughly consistent with the predictions of [68] based on the 10:1 ratio of anvil mass to cylinder mass in our tests. Although there are only two data points, the experimental data for the reverse Taylor cylinders appears noisier than for the forward cylinders. The expected 2% difference in length was therefore not resolved. Still the general agreement between simulation results and experimental observations is good.

The deformed footprint diameter data for the forward Taylor cylinders shows the expected trend of increasing deformation with increasing impact velocity, but the trend is a bit noisier than the length data. Because the deformed cylinders show some degree of non-axisymmetric deformation, footprint images were used to estimate the diameter

Impact manner	Impact velocity (m/s)	Sim. deformed length (mm)	Sim. deformed foot diameter (mm)
Forward	96.1	31.319	11.058
Forward	110.7	29.919	12.600
Forward	116.2	29.379	13.273
Forward	131.8	27.785	15.369
Forward	141.1	26.786	16.651
Forward	153.1	25.461	18.121
Reverse	115.0	29.924	12.361
Reverse	131.0	28.371	14.242

Table 5: Deformed dimensions of each polycrystalline tin cylinder from forward and reverse Taylor impact simulations.

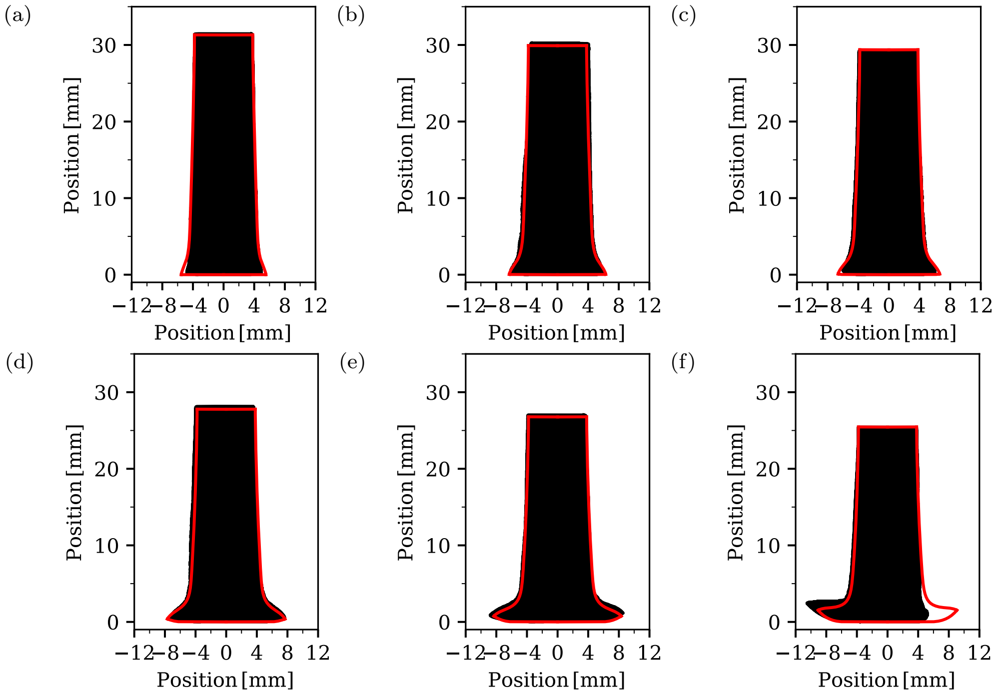

Fig. 16: Comparison of longitudinal profile of deformed specimens after forward impact velocities of 96.1 m/s (a), 110.7 m/s (b), 116.2 m/s (c), 131.8 m/s (d), 141.1 m/s (e), and 153.1 m/s (f). Black profiles correspond to the experiment results; solid red lines indicate simulation results.

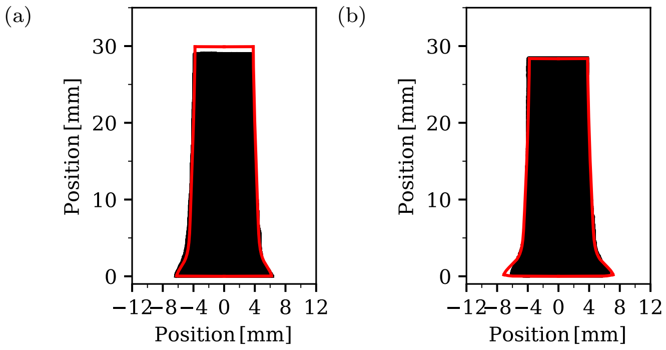

Fig. 17: Comparison of longitudinal profile of deformed specimens after reverse impacts at velocity 115.0 m/s (a) and 131.0 m/s (b). Black profiles correspond to the experiment results, solid red lines indicate simulation results.

range for each experiment. Those ranges are plotted as uncertainty bars on top of the physical measurement of diameter at just one orientation in Fig. 18. Note that physical measurement does not necessarily fall in the center of the range. Also note that diameter measurement for the 153 m/s cylinder that failed was taken from a radial measurement of an intact portion. Since other failed portions of the footprint have less material, that represents something of an upper bound.

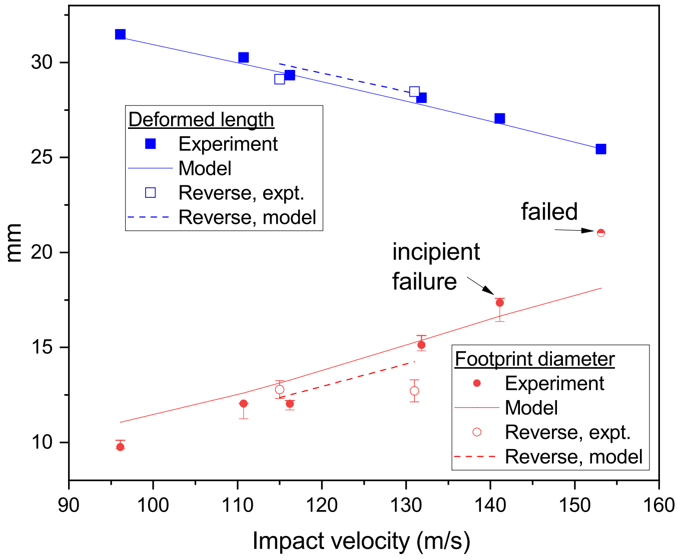

Fig. 18: Simulations using the calibrated PTW strength model agree well with the deformed shapes of both forward and reverse Taylor cylinder tests, aother than the one that failed. The small changes predicted for reverse testing compared to forward were not distinguishable in the data.

Even with scatter in footprint diameter caused by asymmetry, trends in the comparison with the model are evident. The model does not predict the diameters as well as the deformed lengths. For the lowest three velocities of the forward impacts, the model over predicts the diameter by an average of 9%. For the next highest velocity of 131.8 m/s, the deformed diameter matches within uncertainty. The diameter is then underpredicted by several percent for the next highest impact at 141 m/s. Although that cylinder showed some signs of incipient damage, the damage is localized to a couple small regions, and comparing to the model is informative, nonetheless. The diameter of the highest velocity impact is under predicted, but this is expected because the damage is not modeled, so it is not a fair validation test for the strength model. In the lower five impact velocities, the trend going from overprediction to underprediction of the deformed diameters may be related to the increasing amount of plastic deformation with increasing impact velocity. For example, the PTW model slightly overpredicts strain hardening at higher strains because of the effect of the twinning sigmoid on the fit (see high rate fits in Fig. 14), which could lead to underpredicting the deformation at higher impact velocities.

For the reverse Taylor experiments, the model predicts about 8% smaller footprint diameter then the forward impact models. At 115 m/s, the reverse Taylor cylinder diameter was about 6% more than the forward cylinder at 116 m/s, but the difference is within experimental scatter. The diameter of the 131 m/s reverse cylinder is 16% smaller than the 132 m/s forward cylinder, and 12% below the model prediction. The sections in Fig. 5 and the model-experiment comparisons in Fig. 16 and Fig. 17 all indicate the the model generally predicts the shape well all along the length until the very end of the cylinder.

A Physical Regime Sensitivity (PRS) analysis in [69] of a copper Taylor cylinder provides insights into interpreting these results. The deformed length is broadly sensitive to the average strength over the range of strains, strain rates, and temperatures experienced by the cylinder. Thus, the excellent prediction of the deformed length is consistent with the broad agreement of the PTW fit with the constitutive data in Fig. 14 and gives some confidence in extrapolation to the somewhat higher strain rates in the Taylor cylinders.

The footprint diameter, on the other hand, is also sensitive to the shape of the stress-strain curve and the competition between strain hardening and thermal softening [69]. Thus, the diameter predictions are less accurate because the PTW fits in Fig. 14 smooth through the sigmoid caused by twinning and also do not perfectly capture the hardening at higher strains. Furthermore, the high temperatures in the cylinders from plastic work (see section 6) caused re-crystallization in the microstructure, see Fig. 6(b), which can affect the strength through both smaller grains and possible annealing.

Therefore, to get an even better prediction of the deformed cylinder shape, we would likely need a micromechanical model that captures the evolution of twins and the effects of dynamic recrystallization.

The simulated Taylor cylinder profiles were regenerated with the same PTW parameters but using SESAME 2163 and found to be indistinguishable from the Fig. 16 and Fig. 17 profiles generated with SESAME 2162.

6. Melting and Mixed Phase During the Taylor Cylinder Tests

Simulations of the Taylor cylinders revealed that some material reached the melt temperature and simulations without the CMMP were yielding non-physical results. Thus, in this section we examine the temperature profile from the forward Taylor impact simulations, as well as the role of the multi-phase model in predicting physically correct thermomechanical behavior during incipient melt.

The evolution of the final temperature with respect to impact velocities from forward Taylor impact tests is presented in Fig. 19. As the impact velocities increases, the amount of plastic strain localized near the contact surface of the cylinder increases. The associated plastic work leads to local temperature rise. When the melting temperature is reached (~ 503 K) at the contact surface of the tin cylinder, solid tin (in β phase) begins to convert into liquid. In these forward Taylor impact tests, melting starts for impact velocity of 131.8 m/s and above.

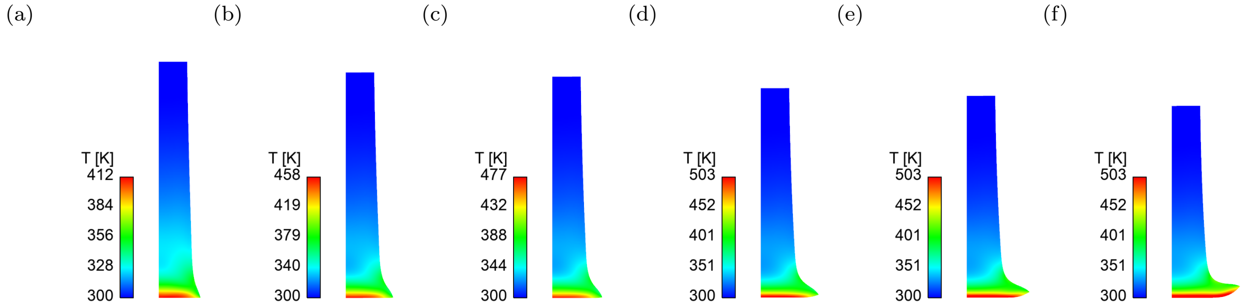

Fig. 19: Temperature profile of deformed specimens after impacts using multi-phase model at velocities 96.1 m/s (a), 110.7 m/s (b), 116.2 m/s (c), 131.8 m/s (d), 141.1 m/s (e), and 153.1 m/s (f).

With the use of the multi-phase model, the solid tin in the β phase is *gradually* converted into the liquid phase as the melting temperature is reached. In other words, the dissipative energy from plastic deformation gradually absorbs the latent heat of fusion, increasing the fraction of the liquid phase, without bringing the local temperature above melting temperature (~ 503 K) unless and until the local material point is fully liquid.

Fig. 20(a) illustrates the transition from β phase to liquid phase of the tin cylinder after impact at 141.1 m/s, using mass fraction contours. The liquid fraction does not exceed 45%, and the CMMP gives a finite strength for the mixed phase material. This gradual transition prevents the *immediate* total loss of material shear strength near the contact surface of the cylinder.

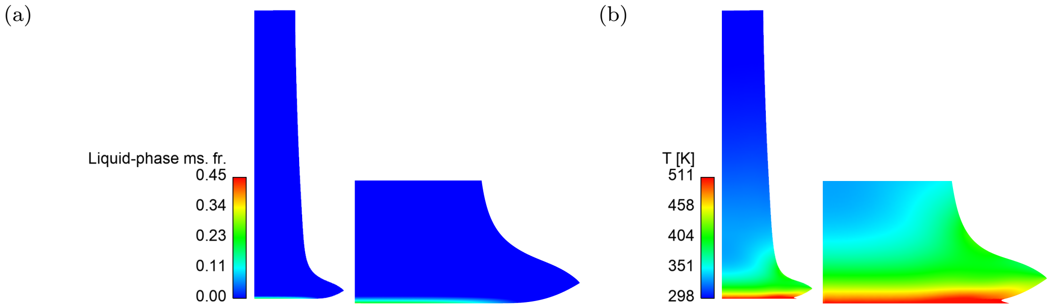

Fig. 20: (a) Using the multi-phase model, the mass fraction of liquid phase never exceeds 45% for the deformed cylinder after impact at a velocity of 141.1 m/s. (b) With a traditional single phase treatment, material points melt at the melt temperature. Without the latent heat of fusion, continued deformation drives the temperature non-physically large. The close-up profile near the contact surface shows that the melted material lost all strength and jetted from the contact surface.

The calculation was repeated using a traditional single-phase treatment of the β phase where crossing the melt line results in instantaneous melt and loss of strength. Fig. 20(b) shows that without the latent heat of fusion in the multi-phase treatment, continued deformation drives the temperature too high, to ~ 511 K near the contact surface of the cylinder. In addition, the suddenly melted tin near the contact surface of the cylinder does not carry any strength and flows freely. Fig. 20(b) shows that the melted material jetted out from the contact surface in the simulation. No such deformation or evidence of melting was observed in the recovered cylinder.

This simulation result highlights the importance of a smoothly-evolving multi-phase and mixed-phase model in predicting a physical evolution of the liquid phase of polycrystalline tin at high strain rates and large plastic deformation.

7. Conclusions and Future Work

This work presents the constitutive ingredients for a CMMP multiphase model for polycrystalline tin. Analytic models for the melt temperature and shear modulus for the solid phases were generated from ab initio calculations based on density functional theory and supplemented by experimental measurements in the β phase. The constitutive behavior of the β phase was characterized with extensive QS and SHPB testing from 87 to 373 K and then used to parameterize a PTW strength model using a Bayesian framework. Multiple forward and reverse Taylor cylinder experiments were performed for validation of the strength model. Simulations using the calibrated CMMP model agreed well with the deformed shapes measured on the Taylor cylinders. Modest discrepancies were likely caused by the inability of PTW to capture micromechanical effects like deformation twinning. The higher impact velocity Taylor cylinders reached the melt temperature in the most highly deformed regions, and the ability of the CMMP model to capture the mixed solid-liquid behavior proved instrumental in getting accurate prediction of their deformed shapes. The PTW model parameters for the β phase were shown to work well with either the SESAME 2162 or 2163 SESAME multiphase EOS.

Additional work is in progress to use this foundation to build a more extensive multi-phase model. First, the β-phase strength is being probed in more extreme conditions using Richtmyer-Meshkov instability (RMI) experiments for extreme strain rates [70], hole closure experiments [71] for higher strains at high rates, and pulsed-power ramp-release experiments [3] for higher pressures. RMI experiments are also probing high-rate strength up into the γ-phase. The ramp-release experiments are extending up into the γ and δ phases. Finally, laser-drive Rayleigh-Taylor experiments [4] are probing simultaneous high-rate and high-pressure strength in the δ-phase.

Supplementary Material

True Stress versus True Strain Data

The true stress versus true strain data for each of the 21 experiments (presented in Fig. 4) is provided as a text file. The titles of these 21 files reflect the corresponding loading conditions (i.e. temperature and strain rate).

Deformed Shape of the Taylor Cylinder after Impact Experiments

After the impact experiments, the cylinder specimens were sectioned along the cylinder length for examination of the deformed shapes and microstructure. Shadowgraphs were taken from the sectioned cylinders. The obtained shadowgraphs were digitized to correlate each pixel in the raw images with a spatial position of corresponding X (in radial direction) and Y (in cylinder length direction) coordinates. The spatial position of every pixel is then used for a direct comparison between the deformed cylinder shapes from experiments and corresponding simulations. The index of each pixel and its spatial position (noted as X and Y, in mm) for each of the eight impact experiments (presented in Figs. 16 and 17) is provided in the supplemental material as a text file. The titles of these eight files reflect the corresponding impact velocity and impact direction (forward versus reverse).

Acknowledgement

This work was supported by the US Department of Energy through the Los Alamos National Laboratory. Los Alamos National Laboratory is operated by Triad National Security, LLC, for the National Nuclear Security Administration of U.S. Department of Energy (Contract No. 89233218CNA000001). Portions of this work were performed at HPCAT (Sector 16), Advanced Photon Source (APS), Argonne National Laboratory. HPCAT operations are supported by DOE-NNSA's Office of Experimental Sciences. The Advanced Photon Source is a U.S. Department of Energy (DOE) Office of Science User Facility operated for the DOE Office of Science by Argonne National Laboratory under Contract No. DE-AC02-06CH11357.

References

1. Rehn, D. A., Greeff, C. W., Burakovsky, L., Sheppard, D. G. & Crockett, S. D. Multiphase tin equation of state using density functional theory. *Physical Review B* **103,** 184102 (2021).
2. Brown, J. *et al.* Experimental evaluation of shear modulus scaling of dynamic strength at extreme pressures. *Journal of Applied Physics* **128** (2020).
3. Brown, J., Davis, J.-P. & Seagle, C. Multi-megabar dynamic strength measurements of Ta, Au, Pt, and Ir. *Journal of Dynamic Behavior of Materials* **7,** 196–206 (2021).
4. Remington, B. A. *et al.* Rayleigh–Taylor instabilities in high-energy density settings on the National Ignition Facility. *Proceedings of the National Academy of Sciences* **116,** 18233–18238 (2019).

5. Anderson, W. W. *et al. Phase transition and spall behavior in β-tin* in *AIP Conference Proceedings* **505** (2000), 443–446.
6. Mabire, C. & Hereil, P. L. *Shock induced polymorphic transition and melting of tin* in *AIP Conference Proceedings* **505** (2000), 93–96.
7. Cox, G. *A Multi-Phase Equation of State and Strength Model for Tin* in *AIP conference proceedings* **845** (2006), 208–211.
8. Buy, F., Voltz, C. & Llorca, F. *Thermodynamically based equation of state for shock wave studies: application to the design of experiments on tin* in *AIP Conference Proceedings* **845** (2006), 41–44.
9. De Rességuier, T. *et al.* Experimental investigation of liquid spall in laser shock-loaded tin. *Journal of applied physics* **101,** 013506 (2007).
10. Hu, J., Zhou, X., Dai, C., Tan, H. & Li, J. Shock-induced bct-bcc transition and melting of tin identified by sound velocity measurements. *Journal of Applied Physics* **104,** 083520 (2008).
11. Buttler, W. *et al.* Second shock ejecta measurements with an explosively driven two-shockwave drive. *Journal of Applied Physics* **116,** 103519 (2014).
12. Schill, W., Austin, R., Brown, J. & Barton, N. Anelasticity and Phase Transition During Ramp-Release in Tin. *Journal of Dynamic Behavior of Materials,* 1–10 (2020).
13. Robert, G., Pillon, L., Seisson, G. & Chauvin, C. *Full multiphase description of materials: Application on tin* in *AIP Conference Proceedings* **2272** (2020), 070040.
14. La Lone, B. *et al.* Release path temperatures of shock-compressed tin from dynamic reflectance and radiance measurements. *Journal of Applied Physics* **114** (2013).
15. Mackay, K. *et al.* Hydrodynamic computations of high-power laser drives generating metal ejecta jets from surface grooves. *Journal of Applied Physics* **128** (2020).
16. Liu, Y. & Grieves, B. Ejecta production and transport from a shocked Sn coupon. *Journal of Fluids Engineering* **136,** 091202 (2014).
17. Zhernokletov, M. V. *et al.* Measurement of the sound velocities behind the shock wave front in tin. *Combustion, Explosion, and Shock Waves* **48,** 112–118 (2012).
18. Hai-Feng, S., Hai-Feng, L., Guang-Cai, Z. & Yan-Hong, Z. Numerical simulation of wave propagation and phase transition of Tin under shock-wave loading. *Chinese Physics Letters* **26,** 066401 (2009).
19. Barton, N. R. *et al.* A Multi-Phase Modeling Framework Suitable for Dynamic Applications. *Metals* **12,** 1844 (2022).
20. Rehn, D. A. *SESAME 2163: an updated tin equation of state* tech. rep. (Los Alamos National Lab.(LANL), Los Alamos, NM (United States), 2023).
21. Davis, J.-P. & Hayes, D. B. *MEASUREMENT OF THE DYNAMIC β-γ PHASE BOUNDARY IN TIN* in *AIP Conference Proceedings* **955** (2007), 159–162.
22. Greeff, C. W. A model for phase transitions under dynamic compression. *Journal of Dynamic Behavior of Materials* **2,** 452–459 (2016).
23. Steinberg, D., Cochran, S. & Guinan, M. A constitutive model for metals applicable at high-strain rate. *Journal of applied physics* **51,** 1498–1504 (1980).
24. Preston, D. L. & Wallace, D. C. A model of the shear modulus. *Solid state communications* **81,** 277–281 (1992).
25. Preston, D. L., Tonks, D. L. & Wallace, D. C. Model of plastic deformation for extreme loading conditions. *Journal of applied physics* **93,** 211–220 (2003).
26. Burakovsky, L., Greeff, C. W. & Preston, D. L. Analytic model of the shear modulus at all temperatures and densities. *Physical Review B* **67,** 094107 (2003).
27. Burakovsky, L., Luscher, D. J., Preston, D., Sjue, S. & Vaughan, D. Generalization of the unified analytic melt-shear model to multi-phase materials: Molybdenum as an example. *Crystals* **9,** 86 (2019).
28. Martinez, E. & Servas, J.-M. *Sound velocity doppler laser interferometry measurements on Tin* in *AIP Conference Proceedings* **620** (2002), 1200–1203.
29. Sturtevant, B. T., Pantea, C. & Sinha, D. N. Evaluation of the transmission line model for couplant layer corrections in pulse-echo measurements. *IEEE transactions on ultrasonics, ferroelectrics, and frequency control* **60,** 943–953 (2013).
30. Sturtevant, B. T., Velisavljevic, N., Sinha, D. N., Kono, Y. & Pantea, C. A broadband wavelet implementation for rapid ultrasound pulse-echo time-of-flight measurements. *Review of Scientific Instruments* **91** (2020).

31. Cedrone, N. P. & Curran, D. Electronic pulse method for measuring the velocity of sound in liquids and solids. *The Journal of the Acoustical Society of America* **26,** 963–966 (1954).

32. Allen, D., Rule, W. & Jones, S. Optimizing material strength constants numerically extracted from Taylor impact data. *Experimental mechanics* **37,** 333–338 (1997).

33. Rule, W. K. A numerical scheme for extracting strength model coefficients from Taylor test data. *International journal of impact engineering* **19,** 797–810 (1997).

34. Hernandez, C., Maranon, A., Ashcroft, I. & Casas-Rodriguez, J. A computational determination of the Cowper–Symonds parameters from a single Taylor test. *Applied Mathematical Modelling* **37,** 4698–4708 (2013).

35. Maudlin, P., Bingert, J., House, J. & Chen, S. On the modeling of the Taylor cylinder impact test for orthotropic textured materials: experiments and simulations. *International Journal of Plasticity* **15,** 139–166 (1999).

36. Plunkett, B., Cazacu, O., Lebensohn, R. & Barlat, F. Elastic-viscoplastic anisotropic modeling of textured metals and validation using the Taylor cylinder impact test. *International Journal of Plasticity* **23,** 1001–1021 (2007).

37. Nguyen, T., Fensin, S. J. & Luscher, D. J. Dynamic crystal plasticity modeling of single crystal tantalum and validation using Taylor cylinder impact tests. *International Journal of Plasticity* (2021).

38. Scott, N. R., Nelms, M. D. & Barton, N. R. Assessment of reverse gun taylor cylinder experimental configuration. *International Journal of Impact Engineering* **149,** 103772 (2021).

39. See Supplemental Material at [URL will be inserted by publisher] for the stress-strain data (from Figure 4) and the deformed Taylor cylinder shapes (from Figures 16 and 17).

40. Schneider, M. S. *et al.* Laser shock compression of copper and copper–aluminum alloys. *International journal of impact engineering* **32,** 473–507 (2005).

41. Chen, C. *et al.* Interplay of dislocation slip and deformation twinning in tantalum at high strain rates. *Scripta Materialia* **69,** 709–712 (2013).

42. Zhao, F. *et al.* Macrodeformation twins in single-crystal aluminum. *Physical review letters* **116,** 075501 (2016).

43. Della Ventura, N. M. *et al.* Micromechanical response of pure magnesium at different strain rate and temperature conditions: twin to slip and slip to twin transitions. *Acta Materialia* **243,** 118528 (2023).

44. Kammer, E., Cardinal, L., Vold, C. & Glicksman, M. The elastic constants for single-crystal bismuth and tin from room temperature to the melting point. *Journal of Physics and Chemistry of Solids* **33,** 1891–1898 (1972).

45. Fraizier, E., Nadal, M.-H. & Oltra, R. Noncontact determination of the elastic moduli of β-Sn up and through the melting point. *Journal of applied physics* **93,** 649–654 (2003).

46. Cox, G. *Tabulating a multiphase equation of state* in *AIP Conference Proceedings* **2272** (2020), 070011.

47. Bernard, S. & Maillet, J. First-principles calculation of the melting curve and Hugoniot of tin. *Physical Review B* **66,** 012103 (2002).

48. Hinton, J. K. *et al.* Response of the mode Grüneisen parameters with anisotropic compression: A pressure and temperature dependent Raman study of β-Sn. *Physical Review B* **102,** 184112 (2020).

49. Briggs, R. *et al. Melting of sn to 1 mbar* in *Journal of Physics: Conference Series* **377** (2012), 012035.

50. Briggs, R. *et al.* High-pressure melting behavior of tin up to 105 GPa. *Physical Review B* **95,** 054102 (2017).

51. Briggs, R. *et al.* Coordination changes in liquid tin under shock compression determined using in situ femtosecond x-ray diffraction. *Applied Physics Letters* **115** (2019).

52. Kenamond, M., Bement, M. & Shashkov, M. Compatible, total energy conserving and symmetry preserving arbitrary Lagrangian–Eulerian hydrodynamics in 2D rz–Cylindrical coordinates. *Journal of Computational Physics* **268,** 154–185 (2014).

53. Burakovsky, L., Preston, D. L. & Silbar, R. R. Melting as a dislocation-mediated phase transition. *Physical Review B* **61,** 15011 (2000).

54. Burakovsky, L., Preston, D. L. & Silbar, R. R. Analysis of dislocation mechanism for melting of elements: Pressure dependence. *Journal of Applied Physics* **88,** 6294–6301 (2000).

55. Johnson, G. R. & Cook, W. H. *A constitutive model and data for metals subjected to large strains, high strain rates and high temperatures* in *Proceedings of the 7th International Symposium on Ballistics* **21** (1983), 541–547.

56. Follansbee, P. & Kocks, U. A constitutive description of the deformation of copper based on the use of the mechanical threshold stress as an internal state variable. *Acta Metallurgica* **36,** 81–93 (1988).

57. Chen, S. R. & Gray, G. T. Constitutive behavior of tantalum and tantalum-tungsten alloys. *Metallurgical and Materials Transactions A* **27,** 2994–3006 (1996).

58. Wallace, D. C. Irreversible thermodynamics of overdriven shocks in solids. *Physical Review B* **24,** 5597 (1981).
59. Wallace, D. C. Nature of the process of overdriven shocks in metals. *Physical Review B* **24,** 5607 (1981).
60. Price, M. C., Kearsley, A. T. & Burchell, M. J. Validation of the Preston–Tonks–Wallace strength model at strain rates approaching 1011 s- 1 for Al-1100, tantalum and copper using hypervelocity impact crater morphologies. *International Journal of Impact Engineering* **52,** 1–10 (2013).
61. Prime, M. B. *et al.* A broad study of tantalum strength from ambient to extreme conditions. *Acta Materialia* **231,** 117875. ISSN: 1359-6454. `https://www.sciencedirect.com/science/article/pii/S1359645422002610` (2022).
62. Austin, R. A. & McDowell, D. L. A dislocation-based constitutive model for viscoplastic deformation of fcc metals at very high strain rates. *International Journal of Plasticity* **27,** 1–24 (2011).
63. Austin, R. A. & McDowell, D. L. Parameterization of a rate-dependent model of shock-induced plasticity for copper, nickel, and aluminum. *International Journal of Plasticity* **32- 33,** 134–154 (2012).
64. Gattiker, J., Klein, N., Lawrence, E. & Hutchings, G. LANL/SEPIA: Initial release. Version v1.0.0. `https://doi.org/10.5281/zenodo.3979585` (Aug. 2020).
65. Walters, D. J. *et al.* Bayesian calibration of strength parameters using hydrocode simulations of symmetric impact shock experiments of Al-5083. *Journal of Applied Physics* **124,** 205105 (2018).
66. Nguyen, T., Francom, D. C., Luscher, D. & Wilkerson, J. Bayesian calibration of a physics-based crystal plasticity and damage model. *Journal of the Mechanics and Physics of Solids,* 104284 (2021).
67. Steinberg, D. *et al. Equation of state and strength properties of selected materials* (Lawrence Livermore National Laboratory Livermore, CA, 1996).
68. Liu, J. *et al.* Influence of mass ratio on forward and reverse ballistic impact equivalence: experiments, simulations, and mechanism analysis. *Experimental Mechanics* **57,** 387–404 (2017).
69. Prime, M. B., Merson, J. S. & Chen, S.-R. Physical Regime Sensitivity. *Journal of Dynamic Behavior of Materials* **9,** 248–261 (2023).
70. Prime, M. B. *et al.* Tantalum strength at extreme strain rates from impact-driven Richtmyer-Meshkov instabilities. *Physical Review E* **100,** 053002 (2019).
71. Nelms, M. *et al.* High-rate strength response of tantalum from dynamic hole closure experiments. *Journal of Applied Physics* **132** (2022).